

Enhancement of sulfamethoxazole degradation via efficient heterogeneous activation of peracetic acid by FeS

Linyi Li ¹, Yanlin Wu ^{2*} and Wenbo Dong ^{1,3*}

¹ Shanghai Key Laboratory of Atmospheric Particle Pollution and Prevention, Department of Environmental Science & Engineering, Fudan University, Shanghai 200433, China; 20210740009@fudan.edu.cn

² School of Resources and Environmental Engineering, Shanghai Polytechnic University, Shanghai 201209, China; wuyanlin@fudan.edu.cn

³ Shanghai institute of pollution control and ecological security, Shanghai 200092, China; wbdong@fudan.edu.cn

* Correspondence: W: wuyanlin@fudan.edu.cn; D: wbdong@fudan.edu.cn

Summary

Table S1. Experimental equipments.

Table S2. The Second-order rate constants for reactions between organics and reactive oxygen species (ROS) ($\text{mol}^{-1}\cdot\text{s}^{-1}$).

Table S3. BET surface area, particle size, pore diameter and pore volume of FeS.

Table S4. Comparison of pollutants degradation in PAA system activated by different heterogeneous catalysts.

Table S5. Possible structures of SMX degradation intermediates.

Table S6. Front-line electron density (FED) values for each atom of SMX.

Table S7. The ecotoxicity of SMX identified intermediates predicted by ECOASR.

Table S8. The ecotoxicity of SMX identified intermediates predicted by T.E.S.T.

Text S1. Chemicals.

Text S2. Morphology and structure of synthesized FeS.

Text S3. Preparation procedure of PAA.

Text S4. Determination of PAA and H_2O_2 concentration.

Text S5. Preparation and calibration of KMnO_4 solution.

Text S6. Experimental devices.

Text S7. DFT calculation.

Text S8. Acute and chronic toxicity assessment.

Text S9. The calculation of quenching agents concentration.

Text S10. More details on the discussion of F^- .

Text S11. The reason for the low TOC removal rate.

Figure S1. SEM images of FeS at different magnification.

Figure S2. High-resolution XPS spectrum of (a) Fe 2p, (b) S 2p for FeS; (c) XRD patterns and (d) N_2 adsorption-desorption isotherm curves of FeS.

Figure S3. The pore-size distribution curves of FeS.

Figure S4. The effect of the presence of $20 \mu\text{mol}\cdot\text{L}^{-1}$ H_2O_2 in PAA tested solution on SMX degradation.

Figure S5. Effect of (a) FeS dosage and (b) PAA concentration their degradation corresponding degradation rate constants in FeS/PAA system.

Figure S6. Effect of SMX concentration on (a) SMX degradation and (b) their degradation corresponding degradation rate constants in FeS/PAA system.

Figure S7. Effects of initial pH values on their degradation corresponding degradation rate constants in FeS/PAA system.

Figure S8. The real reaction pH value during FeS/PAA process.

Figure S9. Distribution of PAA as function of pH.

Figure S10. Time-dependent concentration of dissolved Fe(II) in FeS/PAA system.

Figure S11. Residual PAA in the SMX/FeS/PAA system.

Figure S12. (a) The optimized chemical structure of SMX molecular; (b) HOMO and (c) LUMO orbitals of SMX.

Figure S13. The degradation pathways of SMX in FeS/PAA system.

Figure S14. The (a) acute and (b) chronic toxicity of SMX and its TPs.

Figure S15. The TOC removal rate during FeS/PAA oxidation of SMX.

References

Table S1. Experimental equipments.

Instrument or equipments	Model	Manufacturer
Electronic Analytical Balance	AL104	Mettler Toledo, China
Magnetic stirrer	HJ-4	Changzhou Putian Instrument Manufacturing, China
Ultraviolet visible spectrophotometer (UV-vis spectrophotometer)	UV-1900i	Shimadzu, Japan
High performance liquid chromatography (HPLC)	Ultimate 3000	Dionex, USA
Vacuum freeze dryer	LGJ-10	Beijing Songyuan Huaxing Technology Development, China
scanning electron microscope (SEM)	Apereo 2S	Thermo Fisher, USA
X-ray photoelectron spectroscopy (XPS)	K-Alpha	Thermo Fisher Scientific, USA
X-ray diffraction (XRD)	D2 Phaser	Bruker AG, Germany
Micropore Chemisorption Analyzer	ASAP 2460	Micromeritics, USA
Electron spin resonance spectroscopy (ESR)	EMX-PLUS	Bruker AG, Germany
Liquid phase mass spectrometry analyzer (LC-MS)	6200 series TOF/6500 series Q-TOF	Agilent, USA
Total organic carbon analyzer	TOC-L CPH	Shimadzu, Japan

Table S2. The Second-order rate constants for reactions between organics and ROS ($\text{mol}^{-1}\cdot\text{s}^{-1}$).

Chemicals	$k_{\text{HO}\cdot}$	k_{HO_2}	$k_{\text{O}_2\cdot-}$	References
SMX	5.5×10^9	2.0×10^4	na	[1]
MeOH	9.7×10^8	3.0×10^3	na	[1]
CHCl_3	5×10^6	na	3×10^{10}	[2]
FFA	1.5×10^{10}	1.2×10^8	na	[1]
IPA	1.9×10^9	na	na	[1]

Table S3. BET surface area, particle size, pore diameter and pore volume of FeS.

Sample	FeS
BET surface area ($\text{m}^2\cdot\text{g}^{-1}$)	2.4697
Average particle size (nm)	2429.4036
Average pore diameter (nm)	14.9538
Total pore volume ($\text{cm}^3\cdot\text{g}^{-1}$)	0.012024

Table S4. Comparison of pollutants degradation in PAA system activated by different heterogeneous catalysts.

System	Pollutant	Initial concentration	Catalyst dosage	PAA dosage	Reaction time	Initial pH	Degradation rate	Reference
FeS/PAA	SMX	$5 \mu\text{mol}\cdot\text{L}^{-1}$	$50 \text{mg}\cdot\text{L}^{-1}$	$200 \mu\text{mol}\cdot\text{L}^{-1}$	5 min	5.5	100%	this study
CuS/PAA	TC	$10 \mu\text{mol}\cdot\text{L}^{-1}$	$50 \text{mg}\cdot\text{L}^{-1}$	$100 \mu\text{mol}\cdot\text{L}^{-1}$	30 min	7.0	70.8%	[3]
nCuO/PAA	CBZ	$4.23 \mu\text{mol}\cdot\text{L}^{-1}$	$40 \text{mg}\cdot\text{L}^{-1}$	$520 \mu\text{mol}\cdot\text{L}^{-1}$	30 min	7.0	AP 90%	[4]
nCo ₃ O ₄ /PAA	CBZ	$4.23 \mu\text{mol}\cdot\text{L}^{-1}$	$40 \text{mg}\cdot\text{L}^{-1}$	$520 \mu\text{mol}\cdot\text{L}^{-1}$	30 min	7.0	AP 58%	[4]
nFe ₃ O ₄ /PAA	CBZ	$4.23 \mu\text{mol}\cdot\text{L}^{-1}$	$40 \text{mg}\cdot\text{L}^{-1}$	$520 \mu\text{mol}\cdot\text{L}^{-1}$	30 min	7.0	AP 11%	[4]
Co ₃ O ₄ /PAA	Orange G	$50 \mu\text{mol}\cdot\text{L}^{-1}$	$100 \text{mg}\cdot\text{L}^{-1}$	$500 \mu\text{mol}\cdot\text{L}^{-1}$	90 min	7.0	100%	[5]
Fe ₃ O ₄ /PAA	SMX	$5 \mu\text{mol}\cdot\text{L}^{-1}$	$1000 \text{mg}\cdot\text{L}^{-1}$	$3000 \mu\text{mol}\cdot\text{L}^{-1}$	90 min	7.03	69.9%	[6]
CuCo ₂ O ₄ /PAA	BPA	$88 \mu\text{mol}\cdot\text{L}^{-1}$	$200 \text{mg}\cdot\text{L}^{-1}$	$400 \mu\text{mol}\cdot\text{L}^{-1}$	60 min	7.0	92.3%	[7]
CuO/PAA	BPA	$88 \mu\text{mol}\cdot\text{L}^{-1}$	$200 \text{mg}\cdot\text{L}^{-1}$	$400 \mu\text{mol}\cdot\text{L}^{-1}$	60 min	7.0	AP 10%	[7]
CoFe ₂ O ₄ /PAA	SMX	$10 \mu\text{mol}\cdot\text{L}^{-1}$	$100 \text{mg}\cdot\text{L}^{-1}$	$200 \mu\text{mol}\cdot\text{L}^{-1}$	30 min	7.0	74.7%	[8]
Co ₃ O ₄ /PAA	SMX	$10 \mu\text{mol}\cdot\text{L}^{-1}$	$100 \text{mg}\cdot\text{L}^{-1}$	$200 \mu\text{mol}\cdot\text{L}^{-1}$	30 min	7.0	12.4%	[8]
Co ₂ O ₃ /PAA	SMX	$10 \mu\text{mol}\cdot\text{L}^{-1}$	$100 \text{mg}\cdot\text{L}^{-1}$	$200 \mu\text{mol}\cdot\text{L}^{-1}$	30 min	7.0	23.8%	[8]

Table S5. Possible structures of SMX degradation intermediates.

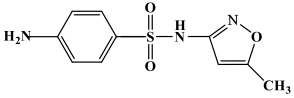
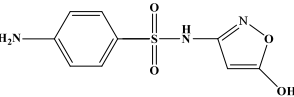
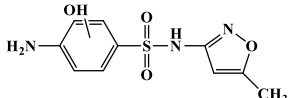
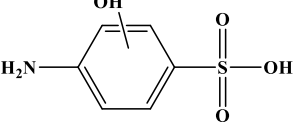
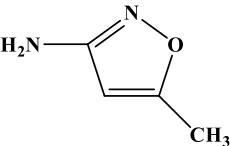
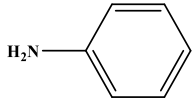
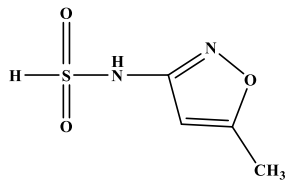
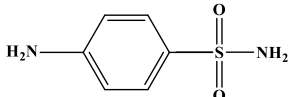
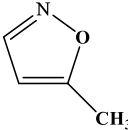
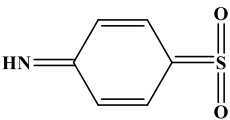
Chemical	Retention time	Detected mass	Molecular formula	Possible structure
SMX	4.371	253.2707	C ₁₀ H ₁₁ N ₃ O ₃ S	
P1	4.429	255.0637	C ₉ H ₉ N ₃ O ₄ S	
P2	4.265	270.0562	C ₁₀ H ₁₂ N ₃ O ₄ S	
P3	0.680	189.0744	C ₆ H ₈ NO ₄ S	
P4	14.454	98.0483	C ₄ H ₆ N ₂ O	
P5	12.891	93.0971	C ₆ H ₇ N	
P6	6.927	162.0158	C ₄ H ₆ N ₂ O ₃ S	
P7	4.559	171.5856	C ₆ H ₈ N ₂ O ₂ S	
P8	5.361	83.0827	C ₄ H ₅ NO	
P9	0.837	155.005	C ₆ H ₅ NO ₂ S	

Table S6. Front-line electron density (FED) values for each atom of SMX.

Atom	2FED ² (HOMO)	2FED ² (LUMO)	FED ² HOMO+FED ² LUMO
1(C)	0.22108	0.36132	0.2912
2(C)	0.19256	0.09808	0.14532
3(C)	0.0704	0.30002	0.18521
4(C)	0.31288	0.3035	0.30819
5(C)	0.07144	0.16494	0.11819
6(C)	0.23466	0.13206	0.18336
7(N)	0.49278	0.14092	0.31685
8(S)	0.04892	0.18414	0.11653
9(O)	0.03226	0.0429	0.03758
10(O)	0.05076	0.04896	0.04986
11(N)	0.06894	0.0477	0.05832
12(C)	0.0184	0.023	0.0207
13(C)	0.00244	0.00398	0.00321
14(C)	0.00678	0.00542	0.0061
15(O)	0.01298	0.01052	0.01175
16(N)	0.03852	0.01908	0.0288
17(C)	0.00114	0.00096	0.00105
18(H)	0.01376	0.00552	0.00964
19(H)	0.00318	0.033	0.01809
20(H)	0.00342	0.01556	0.00949
21(H)	0.0173	0.01228	0.01479
22(H)	0.03892	0.01932	0.02912
23(H)	0.03914	0.0173	0.02822
24(H)	0.00566	0.0062	0.00593
25(H)	0.00052	0.00224	0.00138
26(H)	0.00054	0.0004	0.00047
27(H)	0.00056	0.00052	0.00054
28(H)	0.00006	0.00018	0.00012

*The 2FED²(HOMO) value and 2FED²(LUMO) value was used for the prediction of electrophilic reaction and nucleophilic reaction sites, respectively. And the free radical attack sites were forecasted using FED²(HOMO)+ FED²(LUMO) value.

Table S7. The ecotoxicity of SMX identified intermediates predicted by ECOASR.

Compounds	Acute toxicity (mg·L ⁻¹)				Chronic toxicity (mg·L ⁻¹)			
	Fish (96h-LC50)	Daphnid (48h-LC50)	Green algae (96h-EC50)	Mysid (96h-LC50)	Fish (ChV)	Daphnid (ChV)	Green algae (ChV)	Mysid (ChV)
SMX	267	6.43	21.8	150	5.00	0.068	11.1	15.7
P1	1.26E+3	11.9	48.2	919	36.0	0.114	37.7	189
P2	584	9.08	33.5	370	13.3	0.092	20.9	53.2
P3	1.94E+5	291	1.67E+3	2.38E+5	1.27E+4	2.31	3.01E+3	1.83E+5
P4	270	3.63	13.8	178	6.59	0.036	9.16	28.4
P5	40.3	1.67	5.10	19.4	0.592	0.019	2.04	1.38
P6	2.82E+4	1.26E+4	3.50E+3	1.50E+5	2.08E+3	633	538	2.80E+4
P7	854	8.04	32.6	624	24.5	0.077	25.5	128
P8	883	447	208	1.90E+3	75.4	31.7	42.2	237
P9	6.79E+3	3.23E+3	1.15E+3	2.31E+4	538	192	204	3.53E+3

* Not harmful: > 100 mg·L⁻¹; Harmful: 10-100 mg·L⁻¹; Toxic: 1-10 mg·L⁻¹; Very toxic: <1 mg·L⁻¹.

Table S8. The ecotoxicity of SMX identified intermediates predicted by T.E.S.T.

Compounds	Fathead minnow LC50 (96 hr) mg·L ⁻¹	Daphnia magna LC50 (48 hr) mg·L ⁻¹	T. pyriformis IGC50 (48 hr) mg·L ⁻¹	Oral rat LD50 mg·kg ⁻¹	Bioaccumulation factor	Developmental Toxicity	Mutagenicity
SMX	N/A	N/A	N/A	8549.94	17.11	0.85	-0.04
P1	N/A	N/A	N/A	9653.44	0.75	0.89	-0.14
P2	N/A	N/A	N/A	4306.09	3.33	0.83	-0.13
P3	N/A	N/A	N/A	8731.89	1.89	0.60	-0.05
P4	423.50	22.11	853.66	N/A	3.26	0.33	0.39
P5	80.87	2.97	203.18	372.73	5.38	0.53	0.36
P6	N/A	N/A	N/A	N/A	N/A	N/A	N/A
P7	N/A	N/A	N/A	1827.56	1.71	0.47	-0.07
P8	339.36	234.43	1073.99	N/A	6.01	0.29	0.11
P9	N/A	N/A	N/A	N/A	N/A	N/A	N/A

*N/A meant the prediction not given by T.E.S.T.

Text S1. Chemicals.

Sulfamethoxazole (SMX, 98%), Ferrozine ($C_{20}H_{12}N_4Na_2O_6S_2$, 97%), perchloric acid ($HClO_4$, 70-72%), sodium thiosulfate solution ($H_{10}Na_2O_8S_2$, 0.1000 M), sodium sulfide nonahydrate ($Na_2S \cdot 9H_2O$, $\geq 98\%$) were supplied by Aladdin Biochemical Technology Co., Ltd. (Shanghai, China). Hydrogen peroxide (H_2O_2 , $\geq 30\%$), acetate (CH_3COOH , $\geq 99\%$), sulfuric acid (H_2SO_4 , 95.0-98.0%), formic acid ($HCOOH$, $\geq 99\%$), sodium hydroxide ($NaOH$, $\geq 99\%$), iron(II) sulfate heptahydrate ($FeSO_4 \cdot 7H_2O$, $\geq 99\%$), sodium oxalate ($Na_2C_2O_4$, $\geq 99.8\%$), potassium permanganate ($KMnO_4$, $\geq 99.5\%$), soluble starch ($(C_6H_{10}O_5)_n$), potassium iodide (KI , $\geq 99\%$), manganese(II) sulfate monohydrate ($MnSO_4 \cdot H_2O$, $\geq 99\%$), ammonium molybdate tetrahydrate ($(NH_4)_6Mo_7O_{24} \cdot 4H_2O$, $\geq 99\%$), sodium acetate (CH_3COONa , $\geq 99\%$), isopropanol (C_3H_8O , IPA, $\geq 99.7\%$), trichloromethane ($CHCl_3$, 99%) and furfuryl alcohol (FFA, $C_5H_6O_2$, 98%) were purchased from Sinopharm Chemical Reagent Co., Ltd. (China). Methanol ($MeOH$, 99.9%) and acetonitrile (C_2H_3N , 99.9%) were obtained from J&K Scientific company (China). 5,5-Dimethyl-1-Pyrroline-N-Oxide (DMPO, $\geq 99\%$) and 2,2,6,6-tetramethylpiperidine (TEMP, $\geq 99\%$) were provided by Dojindo. All chemical reagents were used as received. All solutions were prepared in ultrapure water with a resistivity of 18.2 M Ω cm.

Text S2. Morphology and structure of synthesized FeS.

The microscopic surface morphology of FeS was characterized by scanning electron microscopy (SEM), and Figure S1(a)-(d) presented the SEM images of FeS at magnifications of 1000X, 2000X, 5000X, and 10,000X. As shown in Figure S1, the surface of FeS synthesized by homogeneous precipitation method exhibited a rough and porous structure with protrusions and wrinkles. Moreover, numerous small worm-like particles were clustered in the grooves, providing additional reaction sites for the attachment of pollutants and free radicals. The observed surface morphology was essentially consistent with that reported in the literature for FeS [9,10].

The surface elemental composition and valence states of FeS was analyzed by X-ray photoelectron spectroscopy (XPS). The high-resolution XPS spectrum of Fe 2p and S 2p were depicted in Figure 2(a) and (b), respectively. Two dominant characteristic peaks at binding energies of 711.58 eV and 724.38 eV in **Figure 2(a)** was assigned to Fe 2p_{3/2} and Fe 2p_{1/2}. In addition, the Fe 2p_{3/2} spectrum could be further deconvoluted into Fe(II) and Fe(III), represented by two subpeaks at 710.78 and 712.94 eV, respectively. For the S 2p in **Figure S2(b)**, the peaks located at 161.93, 163.60, and 165.69 eV could be identified with S²⁻, S₂²⁻ and S_n²⁻. Peaks associated with SO₄²⁻ were displayed at 168.56 and 169.92 eV. The XPS results revealed that the elemental composition and valence state information of FeS were consistent with theoretical expectations.

The crystallinity and internal structure was investigated using X-Ray Diffraction (XRD). As depicted in Figure S2(c), the strong diffraction peaks located at 29.94°, 33.68°, 43.18°, 53.24° and 70.86° were attributed to the crystallographic planes of (100), (101), (102), (110) and (202) as indicated by the standard diffraction pattern (PDF#65-0408). The sharp and intense peaks, with the absence of any additional peaks, indicating the successful synthesis of FeS.

The specific surface area, pore size, and other related structural parameters were measured by micropore chemisorption analyzer. According to the classification recommended by the International Union of Pure and Applied Chemistry (IUPAC) for adsorption isotherms, the isotherm illustrated in **Figure S2(d)** conformed to the characteristics of Type IV adsorption isotherm accompanied by an H3-type hysteresis loop. It could be inferred that FeS lacked a distinct saturation adsorption plateau, suggesting a relatively irregular pore structure. In addition, the pore size distribution obtained from the desorption data using the Barret-Joyner-Halenda (BJH) model was presented in **Figure S3**. Due to

factors such as the connectivity of internal pore channels and the dispersion of pore sizes, the BJH model produced a false peak around 3.8 nm in the desorption branch data. After disregarding the impact of this false peak, the pore size distribution of FeS was concentrated in the range of 5-25 nm, indicating that FeS was a mesoporous material.

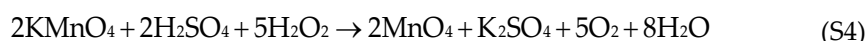
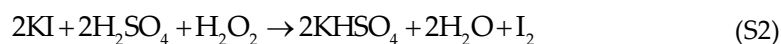
Combining the comprehensive characterization analyses mentioned above, FeS synthesized by homogeneous precipitation method exhibited rough and porous, and the fundamental chemical composition was found to be consistent with literature references, confirming the successful synthesis of FeS.

Text S3. Preparation procedure of PAA.

Briefly, 60 mL CH₃COOH and certain amount of concentrated H₂SO₄ were poured into a 100 mL beaker until H₂SO₄ reached 0.0625 mol·L⁻¹ (existed as catalysts). Heated the mixture in water bath while stirring continuously, maintaining a temperature of around 50 °C. Then added 15 mL 30% H₂O₂ slowly using a Teflon-burette, which might take approximately 90 min. After complete dropwise addition of H₂O₂, the solution should be kept stirring for additional 20 min to ensure thorough reaction. Once the solution was cooled to room temperature, transferred it to a 100 mL brown reagent bottle. The successfully prepared PAA test solution should be stored in a refrigerator for future use.

Text S4. Determination of PAA and H₂O₂ concentration in stock solution.

The concentration of total peroxides (containing both PAA and H₂O₂) and H₂O₂ in stock solution were determined with iodometric method and permanganate titration, respectively [7,11]. The principles were illustrated by Equations (S1)-(S4), and the specific methodology was outlined as follows.



The concentration of total peroxides: In a 250 mL iodometric flask, 40 mL of deionized water cooled to below 10 °C was added, along with 5 mL of 1+9 H₂SO₄ solution and 3 drops of (NH₄)₂MoO₄ solution. Subsequently, a certain volume of the prepared PAA test solution (V₁) and 10 mL of KI solution were introduced. After sealing the flask and shaking it thoroughly, the mixture was placed in the dark for 10 minutes. The solution was then titrated with standard Na₂S₂O₃ solution (c(Na₂S₂O₃)=0.1 mol·L⁻¹). Upon approaching the endpoint (reaching a pale yellow color), 1 mL of starch indicator was added. The titration was continued until the blue color faded away and remained unchanged for 30 seconds, indicating the titration endpoint. The volume of Na₂S₂O₃ standard titrant solution consumed was recorded as V₂.

The concentration of H₂O₂ concentration: In a 250 mL conical flask, 40 mL of deionized water cooled to below 10 °C was added, along with 10 mL of 1+9 H₂SO₄ solution and 3 drops of MnSO₄ solution. After introducing a certain volume of the test solution (V₁), the mixture was shaken gently. Titrated it with KMnO₄ solution (calibrated by Na₂C₂O₄) until the solution turned pale pink. The titration endpoint reached when the color persisted for 30 seconds without fading. Recorded the volume of KMnO₄ solution consumed as V₃.

$$c(\text{PAA}) = \frac{c_2 V_2 - 5 \times c_3 V_3}{2 \times V_1} \quad (\text{S5})$$

$$c(\text{H}_2\text{O}_2) = \frac{5 \times c_3 V_3}{2 \times V_1} \quad (\text{S6})$$

Text S5. Preparation and calibration of KMnO_4 solution.

Preparation of KMnO_4 solution

Approximately 1.6 g KMnO_4 crystals were dissolved in 500 mL of deionized water. Then the beaker covering with a container was heated until boiling, and maintained slight boil for 1 h. After the solution has cooled, transferred it to a 500 mL brown reagent bottle. Set the bottle at room temperature stewing for 2-3 days, a fine-pored glass funnel was used to filter subsequently. The final filtrate was reserved for later calibration and use. Notably, deionized water often contained small amounts of reducing substances that could reduce KMnO_4 to $\text{MnO}_2 \cdot n\text{H}_2\text{O}$, which might accelerate decomposition of H_2O_2 , thus affecting the accuracy of subsequent H_2O_2 concentration measurements potentially. Therefore, heating and filtering of KMnO_4 solution should not be neglected.

Calibration of KMnO_4 solution

$\text{Na}_2\text{C}_2\text{O}_4$ were dried at 105 °C for 2 h. Placed accurate weight of 0.15-0.20 g primary standard $\text{Na}_2\text{C}_2\text{O}_4$ in conical flasks, and added 60 mL deionized water and 15 mL (1+9) H_2SO_4 . Then the flask was heated in water bath to 75-85 °C. Titrated the solution with KMnO_4 while it was hot. In addition, the reaction might proceed slowly unless Mn^{2+} was generated. The titration was continued until the solution turned pale pink and remained unchanged for 30 seconds, indicating the titration endpoint. The volume of KMnO_4 solution consumed was recorded as V_4 . The principle was exhibited as Equation (S7).



Text S6. Experimental devices.

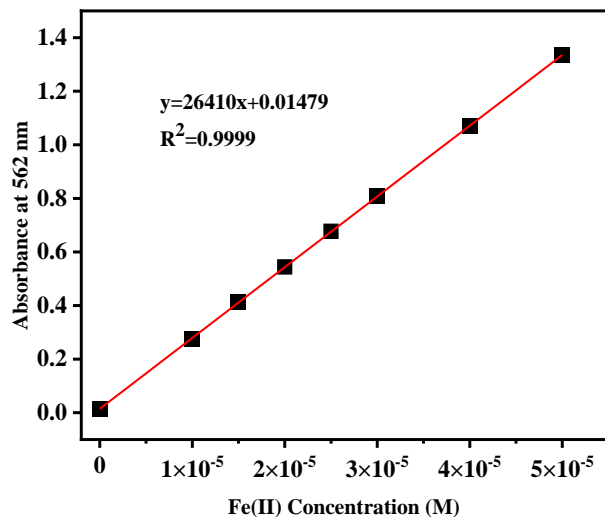
More details on the instruments, characterization methods, and software parameters:

High performance liquid chromatography

SMX was separated from the samples and quantitatively detected by high performance liquid chromatography (HPLC, Dionex Ultimate3000, USA) coupled with XDB-C18 reversed-phase chromatographic column (5 μm \times 4.6 mm \times 150 mm). The wavelength was set at 268 nm, and the sample volume was 20 μL with column temperature of 40 °C. The mobile phase consisted of acetonitrile and formic acid (0.1%) solution, and their volume ratio and flow rate were set at 40: 60 and 1.0 $\text{mL} \cdot \text{min}^{-1}$, respectively. Under above parameters, the absorption peak of SMX appeared around 4.7 min.

Ultraviolet visible spectrophotometer

Transferred the quantitative reaction solution, 2 mL of CH₃COOH-CH₃COONa buffer solution and 2 mL ferrozine solution into colorimetric tube, and diluted to 10 mL scale mark with deionized water. Shaked it to ensure thorough reaction. Stewing for 30 min, the absorbance at $\lambda = 562$ nm was measured and Fe(II) concentration was conversed by calibration curve of Fe(II).



Calibration curve of Fe(II) (Ferrozine-Method).

X-ray photoelectron spectroscopy

The surface elemental composition and valence states of FeS was analyzed by X-ray photoelectron spectroscopy (XPS). The argon ion etching cleaning pretreatment was carried out, and then measured under Al target material in the analysis chamber with vacuum level of 8×10^{-10} Pa. The resulting spectral data were fitted by Avantage software (Thermo Fisher, USA) and reference C 1s (284.6 eV) was used for binding energy calibration.

X-ray diffraction

The crystallinity and internal structure was investigated using X-Ray Diffraction (XRD). The target material is Cu, the accelerating voltage and current was set at 40 KV and 40 mA, respectively. The scanning angle range of wide-angle diffraction was $5-90^\circ$, and the scanning rate was $8^\circ \cdot \text{min}^{-1}$.

Electron spin resonance spectroscopy

Microwave power, 0.99800 mW; modulation frequency, 100 kHz; modulation amplitude, 1 G; sweep width, 5×1 mT; sweep time, 2 min.

Liquid phase mass spectrometry analyzer

The degradation intermediate compounds of SMX were measured by an Agilent 6540 Quadrupole Time-of-Flight (Q-TOF) LC-MS/MS system equipped with a BEH C18 column (2.1×100 mm, $1.7 \mu\text{m}$). For the detection of SMX and its oxidation products, the chromatographic system utilized a mobile phase consisting of MeOH and 0.1% formic acid solution with a flow rate of $0.3 \text{ mL} \cdot \text{min}^{-1}$ and an injection volume of $5 \mu\text{L}$, and its gradient elution conditions were listed in the table below. The ionization was operated in negative ion mode using electrospray ionization (ESI) source. The mass spectrometry scanning

range was set at 50-1000 m/z in the first stage, with the desolvation gas temperature maintained at 350 °C and a flow rate of 12 L·min⁻¹.

Table S9. Gradient elution of UPLC mobile phase.

Time (min)	Mobile phase ratio (MeOH:0.1% formic acid)
0	5:95
1	5:95
8	95:5
13	95:5
14	5:95
15	5:95

Text S7. DFT calculation.

Firstly, the SMX structure was pre-optimized by MM2 method in Chemdraw program. Subsequently, Gaussian 09W and GaussView 5.0.9 were employed for frequency optimization, structural adjustments, and single-point energy calculations. The chosen functional was DFT-B3LYP with a basis set of 6-31G(d,p), and corrections for dispersion were applied based on the research by Grimme et al. [12]. Upon completion of Gaussian calculations, the Multifunctional wavefunction analyzer (Multiwfn 3.8) software was utilized to obtain the values for 2FED²(HOMO), 2FED²(LUMO), and FED²(HOMO)+FED²(LUMO) [13,14]. Among these reactive sites, the sites with a high value of 2FED²(HOMO) and 2FED²(LUMO) were prone to predict electrophilic reaction and nucleophilic reaction, respectively. While the region with a great value of FED²(HOMO)+FED²(LUMO) tended to be hydroxylated by the radical attack. Finally, the structural diagrams were aesthetically enhanced using the visualization software Visual Molecular Dynamics (VMD 1.9.3) program.

Text S8. Acute and chronic toxicity assessment.

The acute and chronic toxicity of SMX and its reaction intermediates to fish, daphnid, green algae and mysid were predicted by using ECOSAR program (version 2.2). The acute toxicity was indicated by the LC₅₀ value (a concentration with 50% mortality of fish and daphnia after 96 h and 48 h of exposure, respectively) and the EC₅₀ value (a concentration with 50% growth inhibition of green algae after 96 h of exposure). The chronic toxicity values (ChV) for aquatic organisms mentioned above were also predicted by the same program. As suggested by Globally Harmonized System of Classification and Labeling of Chemicals (GHS), toxicity was categorized into very toxic (LC₅₀/EC₅₀/ChV ≤ 1 mg·L⁻¹), toxic (1 mg·L⁻¹ < LC₅₀/EC₅₀/ChV ≤ 10 mg·L⁻¹), harmful (10 mg·L⁻¹ < LC₅₀/EC₅₀/ChV ≤ 100 mg·L⁻¹) and not harmful (LC₅₀/EC₅₀/ChV > 100 mg·L⁻¹) [15].

The toxicity was also performed with Toxicity Estimation Software Tool (T.E.S.T.) according to the mathematical models of Quantitative Structure-Activity Relationship (QSAR) (version 5.1.2) [7,16]. The toxicity assessment consisted of the following parameters, primarily including the lethal concentration or dosage of 50% for various organisms (fathead minnow LC₅₀ (96 hr), daphnia magna LC₅₀ (48 hr), T. pyriformis IGC₅₀ (48 hr), oral rat LD₅₀), bioaccumulation factor, developmental toxicity and mutagenicity.

Text S9. The calculation of quenching agents concentration.

The second-order rate constants for reactions between organics and ROS were listed in Table S2. Based on competitive reaction kinetics [17,18], the appropriate concentrations of scavengers were calculated as follows.

IPA was selected as the quencher of HO• due to the high reaction rate ($k_{\text{IPA},\text{HO}\cdot} = 1.9 \times 10^9 \text{ mol}^{-1} \text{ s}^{-1}$). C_{SMX} was $5 \mu\text{mol}\cdot\text{L}^{-1}$ and $k_{\text{SMX},\text{HO}\cdot} = 5.5 \times 10^9 \text{ mol}^{-1}\cdot\text{s}^{-1}$. To assure the complete quenching of HO• produced in selected system, the value of $C_{\text{IPA}}\cdot k_{\text{IPA},\text{HO}\cdot}$ (s^{-1}) needed to be at least 10 or 100 times greater than that of $C_{\text{SMX}}\cdot k_{\text{SMX},\text{HO}\cdot}$. Hence, $5 \text{ mmol}\cdot\text{L}^{-1}$ IPA was enough.

FFA and CHCl_3 were chosen as the scavengers of $^1\text{O}_2$ and $\text{O}_2^{\cdot-}$, respectively. When $10 \mu\text{mol}\cdot\text{L}^{-1}$ FFA was added, the SMX degradation was inhibited, which indicated the contribution from $^1\text{O}_2$ in the SMX removal. However, FFA was also able to quench HO• ($k_{\text{FFA},\text{HO}\cdot} = 1.5 \times 10^{10} \text{ mol}^{-1}\cdot\text{s}^{-1}$), so $0.1 \mu\text{mol}\cdot\text{L}^{-1}$ FFA was used to minimize the competitive consumption of HO•. In a similar way, $0.1 \text{ mmol}\cdot\text{L}^{-1}$ CHCl_3 was chosen.

Text S10. More details on the discussion of F^- .

Fe(III) in solution could form the $[\text{FeF}_6]^{3-}$ complex with Fluoride (F^-), and the coordination number was 6. According to the amount of Fe(II) leaching of $100 \mu\text{mol}\cdot\text{L}^{-1}$ in 5 min (Figure S10), the most extreme case, the leached Fe(II) was oxidized to Fe(III), at this time the concentration of Fe(III) in the solution was $100 \mu\text{mol}\cdot\text{L}^{-1}$. When $2.0 \text{ mmol}\cdot\text{L}^{-1}$ NaF was added to the reaction system, $0.6 \text{ mmol}\cdot\text{L}^{-1}$ F^- formed the complex with Fe(III), and there were still enough F^- to play the role of adsorption of HO• bound on solid surface.

Text S11. The reason for the low TOC removal rate.

On one hand, unlike systems dominated by inorganic oxidants like PS or H_2O_2 , the initial TOC value included the organic carbon both in target pollutant and PAA in PAA-activated systems. In selected SMX/FeS/PAA system, both SMX and PAA were sources of TOC. For TOC removal rate analysis, if $5 \mu\text{mol}\cdot\text{L}^{-1}$ SMX and $200 \mu\text{mol}\cdot\text{L}^{-1}$ PAA was still continued to use, the initial TOC value would be too small to be accurately detected. The concentration of all reactants was thus increased fivefold to raise the initial TOC value. One of the things that had to be considered was that as the concentration of the reactants expanded, the kinetics of the degradation reaction might change. That was to say, we could only balance the accuracy of the instrument and the enlargement of the concentration to obtain a reference TOC removal rate. The removal rate of TOC was not discussed in other PAA degradation systems, which might also be due to what has been discussed above. On the other hand, there were some study verified a TOC reduction as low as our paper. According to Bi et al., [19], the removal rate of TOC was almost 7% after 1 h simulated solar light irradiation in OTC/ Cu^{2+} /PS system (Experimental conditions: $[\text{OTC}]_0=40 \mu\text{mol}\cdot\text{L}^{-1}$, $[\text{Cu}^{2+}]_0=60 \mu\text{mol}\cdot\text{L}^{-1}$, $[\text{PS}]_0=70 \mu\text{mol}\cdot\text{L}^{-1}$, UV 254 light irradiation). Well, UV was usually regarded as one of the powerful approaches to apply energy for activation. It could be inferred that in the UV-based activation systems, the removal rate of TOC would also be more efficient. Combined with the above analysis, the TOC removal rate of about 7% in this study should be reasonable.

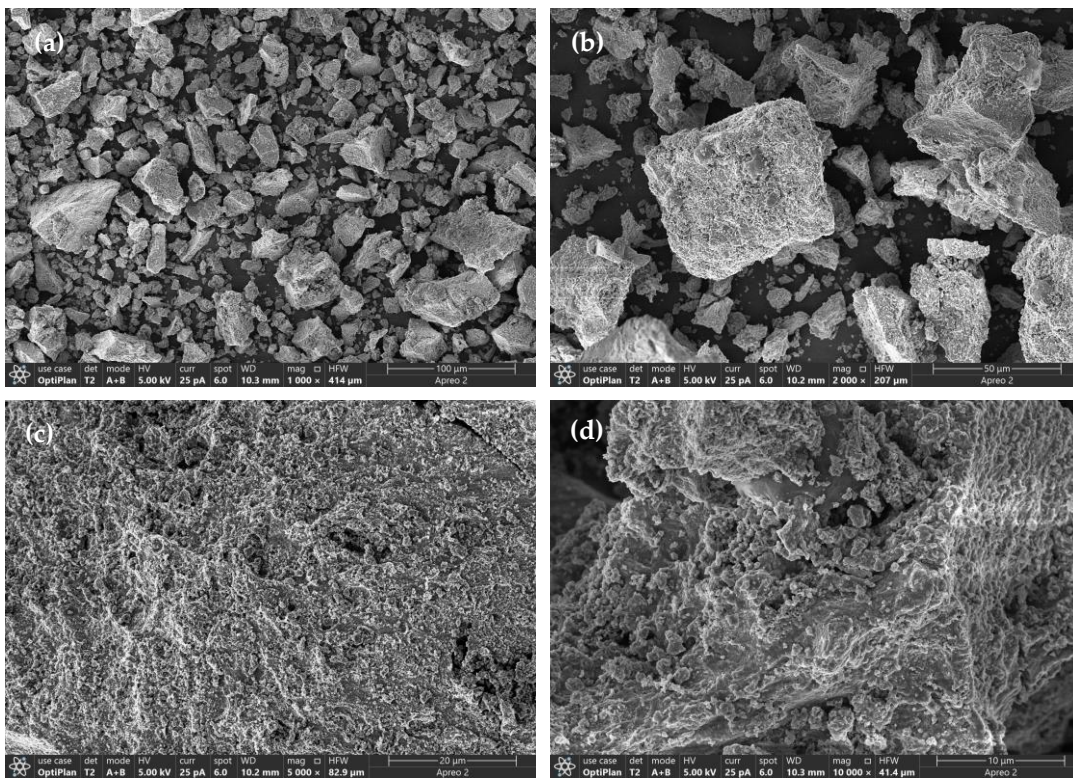


Figure S1. SEM images of FeS at different magnification.

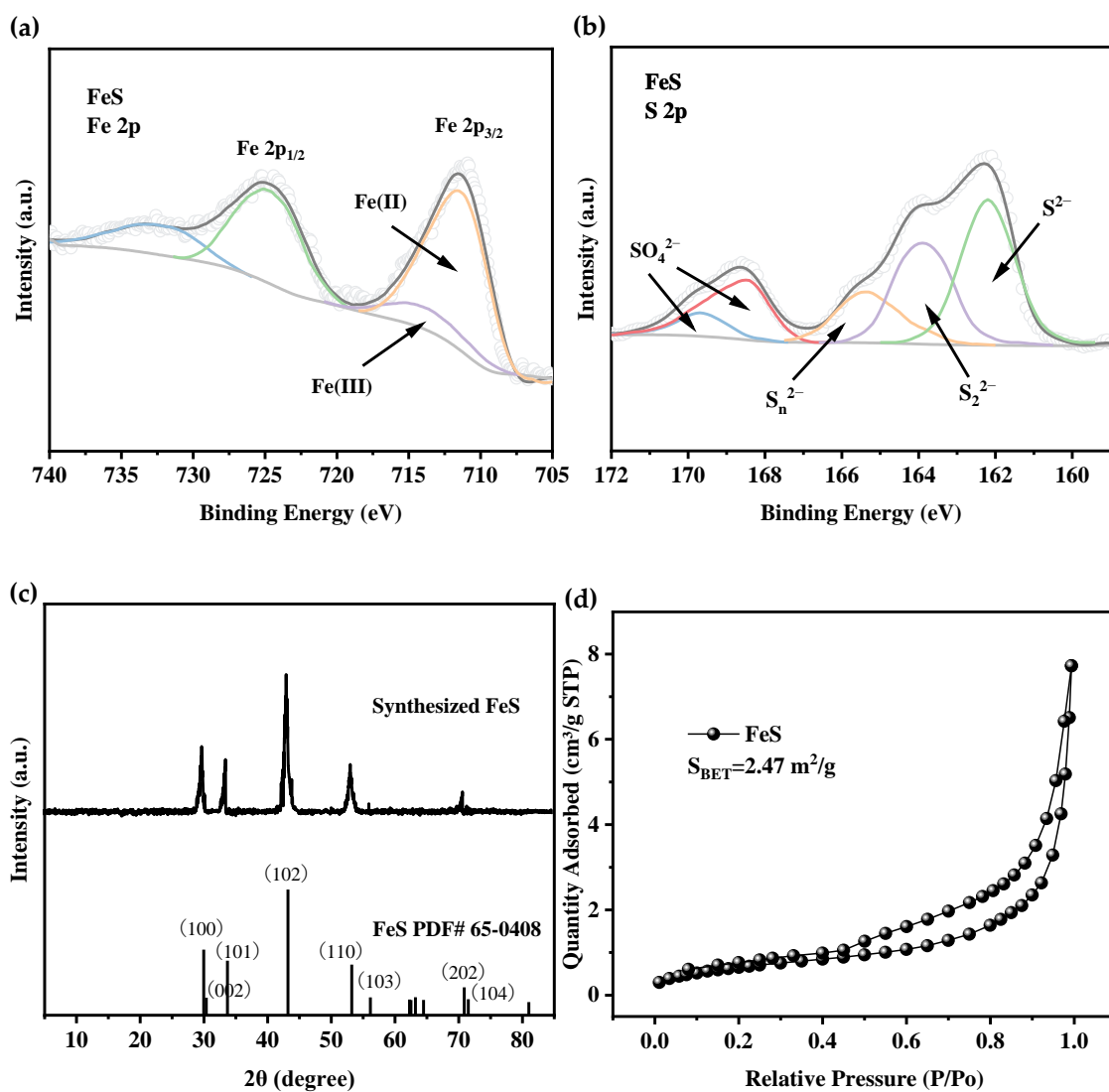


Figure S2. High-resolution XPS spectrum of (a) Fe 2p, (b) S 2p for FeS; (c) XRD patterns and (d) N_2 adsorption-desorption isotherm curves of FeS.

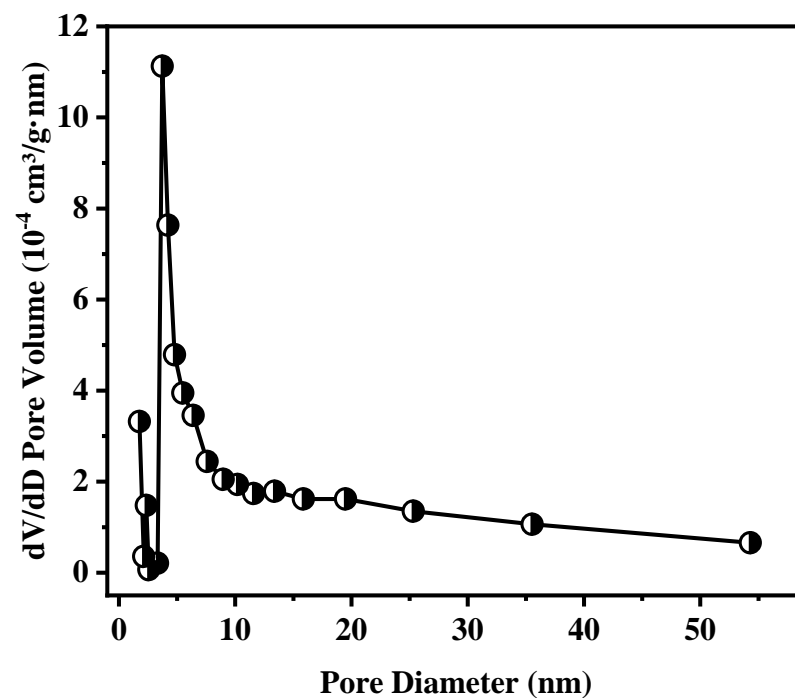


Figure S3. The pore-size distribution curves of FeS.

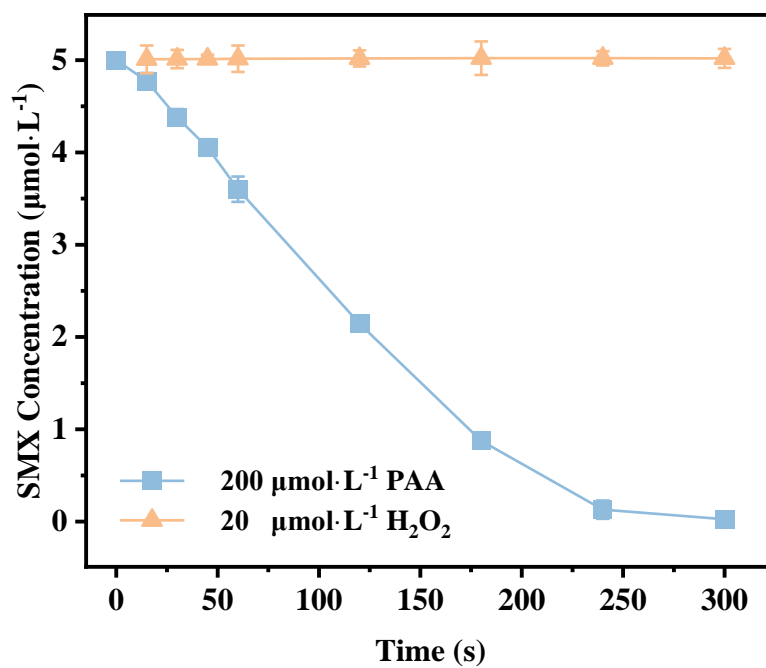


Figure S4. The effect of the presence of $20 \mu\text{mol}\cdot\text{L}^{-1} \text{H}_2\text{O}_2$ in PAA tested solution on SMX degradation. Experimental conditions: $[\text{SMX}]_0 = 5 \mu\text{mol}\cdot\text{L}^{-1}$, $[\text{FeS}]_0 = 50 \text{mg}\cdot\text{L}^{-1}$, $[\text{PAA}]_0 = 200 \mu\text{mol}\cdot\text{L}^{-1}$, $[\text{H}_2\text{O}_2]_0 = 20 \mu\text{mol}\cdot\text{L}^{-1}$, $\text{pH} = 5.5$.

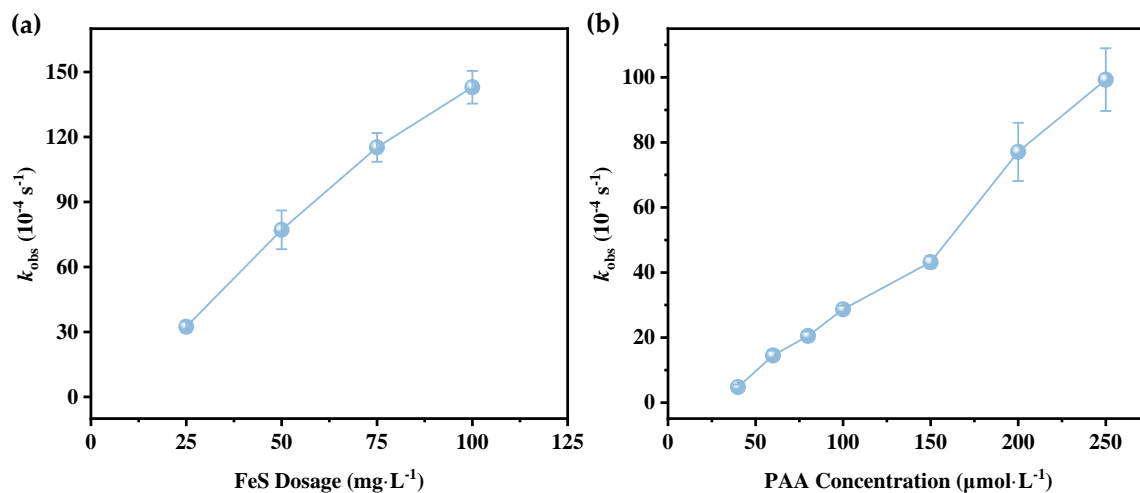


Figure S5. Effect of (a) FeS dosage and (b) PAA concentration on their degradation corresponding degradation rate constants in FeS/PAA system. Experimental conditions for (a): $[\text{SMX}]_0 = 5 \mu\text{mol} \cdot \text{L}^{-1}$, $[\text{PAA}]_0 = 200 \mu\text{mol} \cdot \text{L}^{-1}$, $\text{pH} = 5.5$; for (b): $[\text{SMX}]_0 = 5 \mu\text{mol} \cdot \text{L}^{-1}$, $[\text{FeS}]_0 = 50 \text{mg} \cdot \text{L}^{-1}$, $\text{pH} = 5.5$.

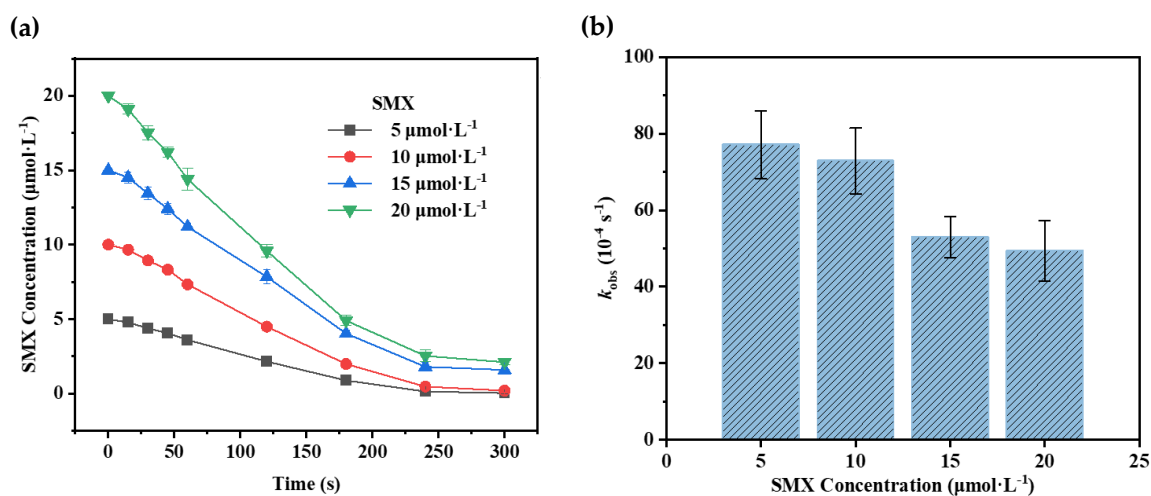


Figure S6. Effect of SMX concentration on (a) SMX degradation and (b) their degradation corresponding degradation rate constants in FeS/PAA system. Experimental conditions: $[\text{FeS}]_0 = 50 \text{mg} \cdot \text{L}^{-1}$, $[\text{PAA}]_0 = 200 \mu\text{mol} \cdot \text{L}^{-1}$, $\text{pH} = 5.5$.

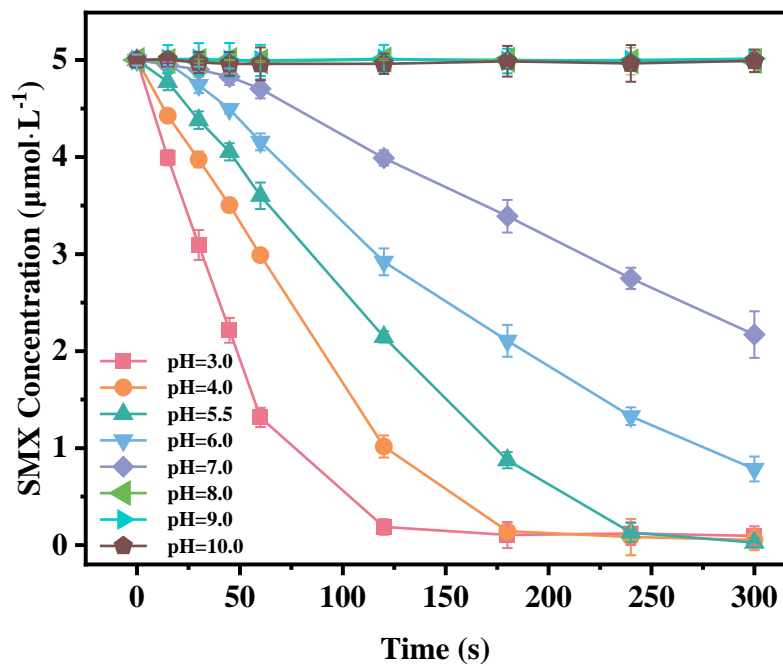


Figure S7. Effects of initial pH values on SMX degradation in FeS/PAA system. Experimental conditions: $[SMX]_0 = 5 \mu\text{mol}\cdot\text{L}^{-1}$, $[\text{FeS}]_0 = 50 \text{ mg}\cdot\text{L}^{-1}$, $[\text{PAA}]_0 = 200 \mu\text{mol}\cdot\text{L}^{-1}$.

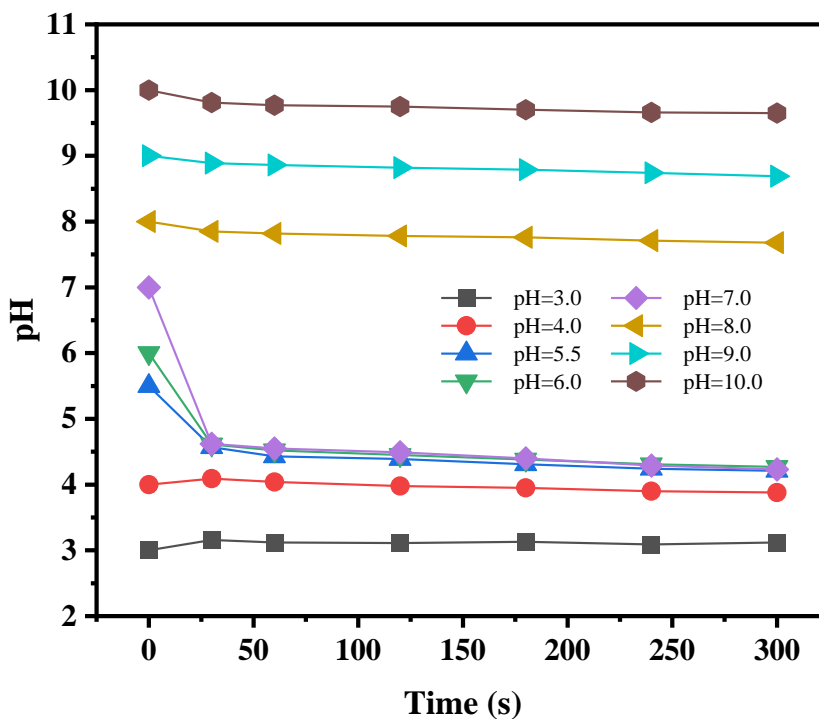


Figure S8. The real reaction pH value during FeS/PAA process.

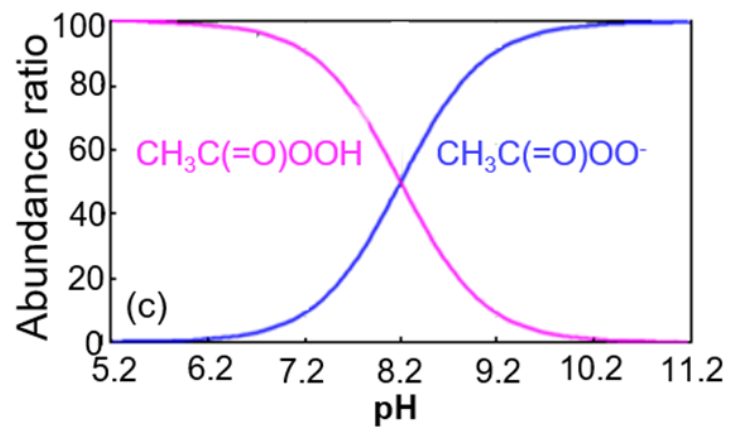


Figure S9. Distribution of PAA as function of pH [20].

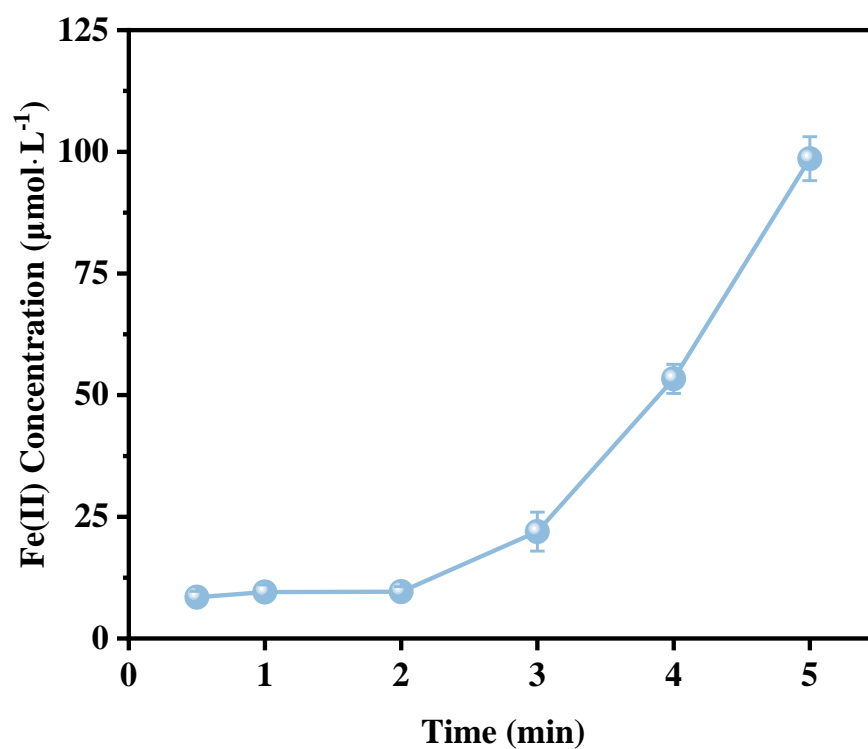


Figure S10. Time-dependent concentration of dissolved Fe(II) in FeS/PAA system. Experimental conditions: $[\text{FeS}]_0 = 50 \text{ mg}\cdot\text{L}^{-1}$, $[\text{PAA}]_0 = 200 \text{ }\mu\text{mol}\cdot\text{L}^{-1}$, $\text{pH} = 5.5$.

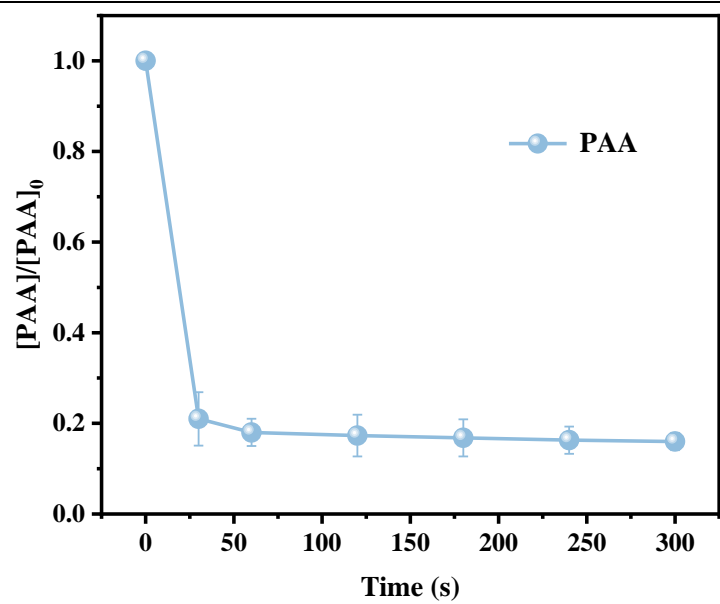


Figure S11. Residual PAA in the SMX/FeS/PAA system. Experimental conditions: $[SMX]_0 = 5 \mu\text{mol}\cdot\text{L}^{-1}$, $[\text{FeS}]_0 = 50 \text{ mg}\cdot\text{L}^{-1}$, $[\text{PAA}]_0 = 200 \mu\text{mol}\cdot\text{L}^{-1}$, $\text{pH} = 5.5$.

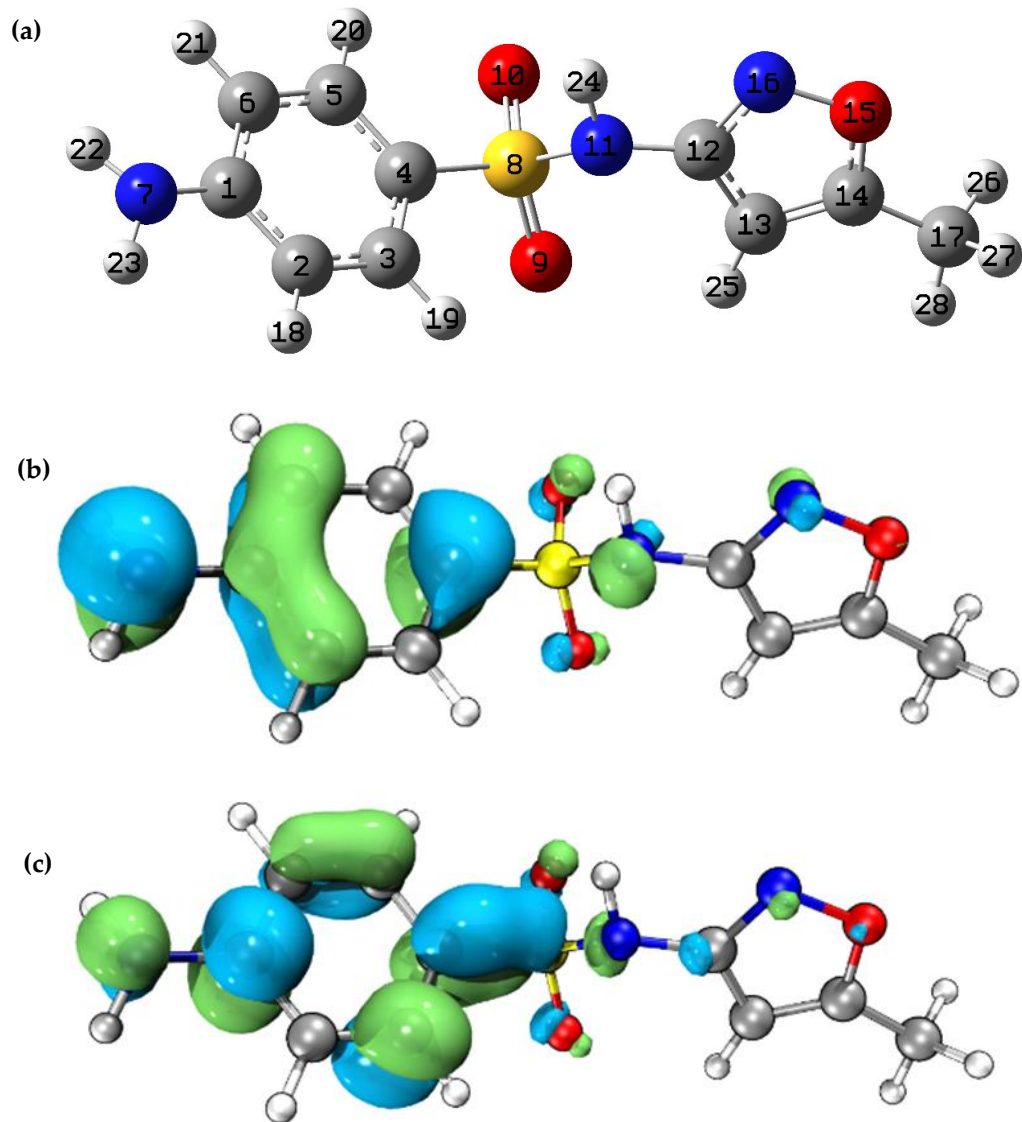


Figure S12. (a) The optimized chemical structure of SMX molecular; (b) HOMO and (c) LUMO orbitals of SMX.

(Dark grey: C atom; Light grey: H atom; Blue: N atom; Red: O atom; Yellow: S atom)

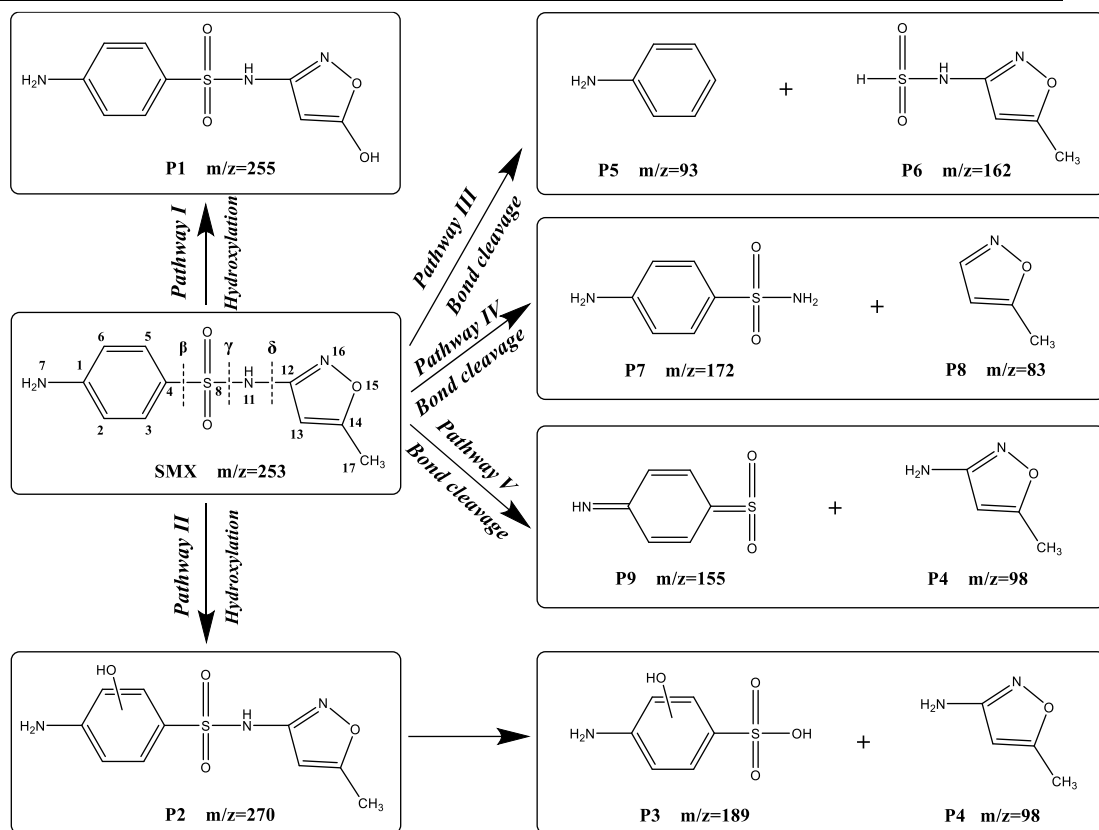
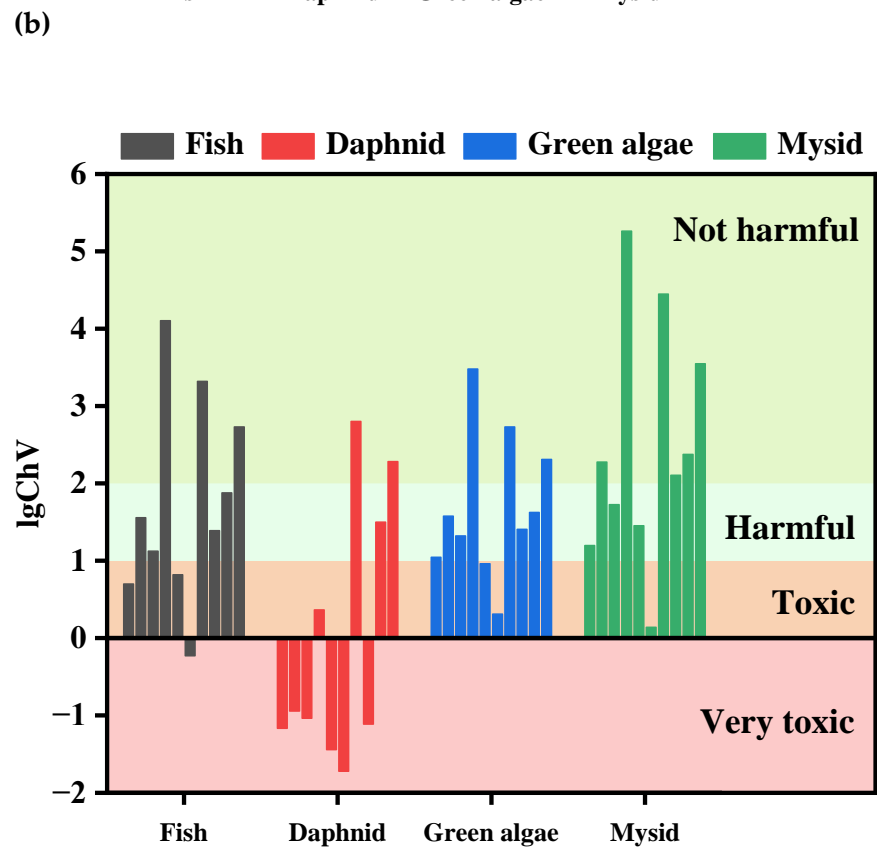
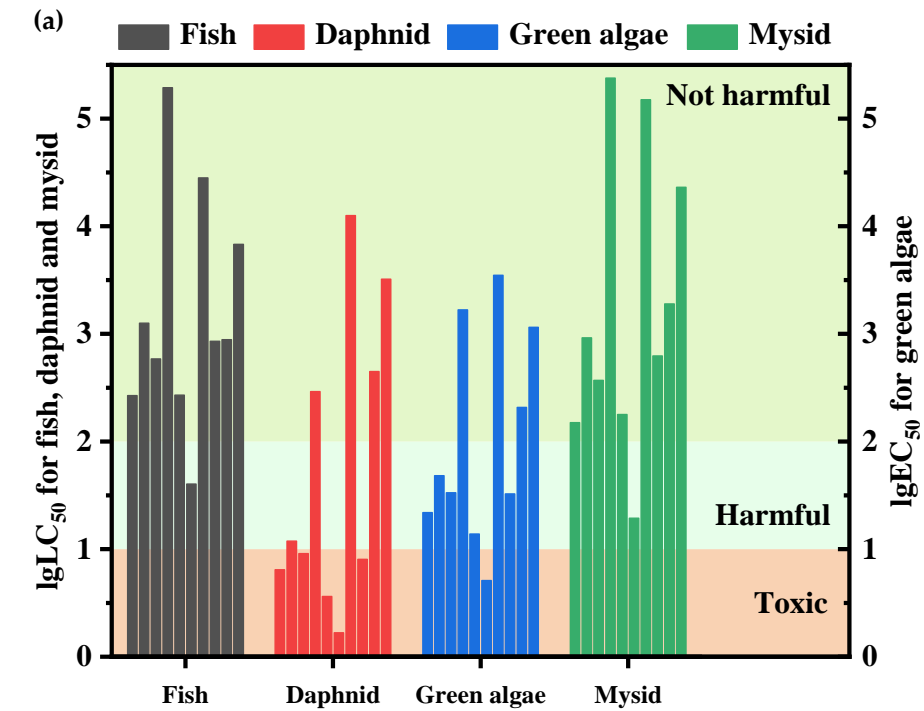


Figure S13. The degradation pathways of SMX in FeS/PAA system.

Figure S14. The (a) acute and (b) chronic toxicity of SMX and its TPs. (*Take the first group of fish



for example: from left to right, ten bars successively stands for SMX and its degradation products.)

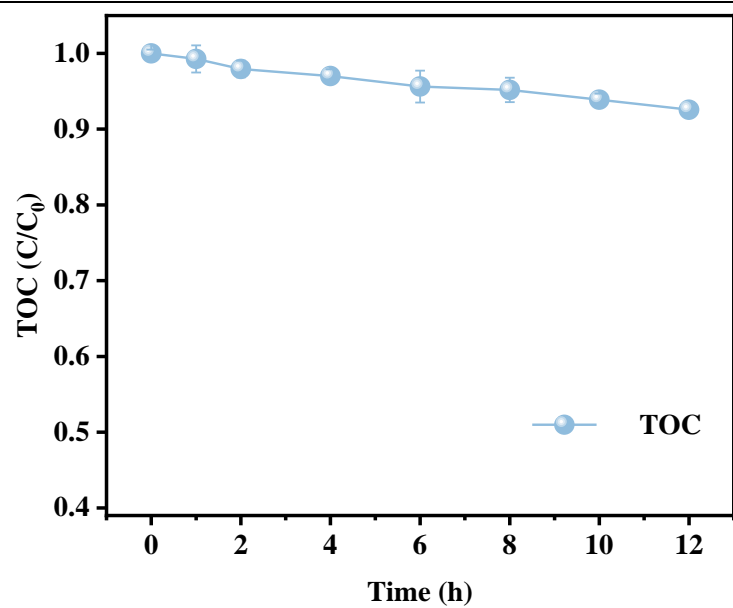


Figure S15. The TOC removal rate during FeS/PAA oxidation of SMX. Experimental conditions: $[\text{SMX}]_0 = 25 \mu\text{mol}\cdot\text{L}^{-1}$, $[\text{FeS}]_0 = 250 \text{mg}\cdot\text{L}^{-1}$, $[\text{PAA}]_0 = 1 \text{mmol}\cdot\text{L}^{-1}$, $\text{pH} = 4.0$.

References

1. Yang, Y.; Banerjee, G.; Brudvig, G.W.; Kim, J.H.; Pignatello, J.J. Oxidation of organic compounds in water by unactivated peroxymonosulfate. *Environ. Sci. Technol.* **2018**, *52*, 5911-5919. <https://doi.org/10.1021/acs.est.8b00735>.
2. Buxton, G.V.; Greenstock, C.L.; Helman, W.P.; Ross, A.B. Critical-review of rate constants for reactions of hydrated electrons, hydrogen-atoms and hydroxyl radicals (OH/O⁻) in aqueous-solution. *J. Phys. Chem. Ref. Data* **1988**, *17*, 513-886. <https://doi.org/10.1063/1.555805>.
3. Chen, J.Y.; Pan, H.J.; Chen, Y.L.; Zhou, Z.M.; Jing, G.H.; Zhao, X.D. Efficient activation of peracetic acid for abatement of tetracycline by W-doped CuS via regulating copper redox cycling. *Chem. Eng. J.* **2023**, *464*, 16. <https://doi.org/10.1016/j.cej.2023.142693>.
4. Zhang, L.L.; Chen, J.B.; Zhang, Y.L.; Xu, Y.; Zheng, T.L.; Zhou, X.F. Highly efficient activation of peracetic acid by nano-CuO for carbamazepine degradation in wastewater: The significant role of H₂O₂ and evidence of acetylperoxy radical contribution. *Water Res.* **2022**, *216*, 10. <https://doi.org/10.1016/j.watres.2022.118322>.
5. Wu, W.; Tian, D.; Liu, T.C.; Chen, J.B.; Huang, T.Y.; Zhou, X.F.; Zhang, Y.L. Degradation of organic compounds by peracetic acid activated with Co₃O₄: A novel advanced oxidation process and organic radical contribution. *Chem. Eng. J.* **2020**, *394*, 8. <https://doi.org/10.1016/j.cej.2020.124938>.
6. Dai, Y.H.; Yang, S.G.; Wu, L.L.; Cao, H.; Chen, L.J.; Zhong, Q.; Xu, C.M.; He, H.; Qi, C.D. Converting peracetic acid activation by Fe₃O₄ from nonradical to radical pathway via the incorporation of L-cysteine. *J. Hazard. Mater.* **2024**, *465*, 10. <https://doi.org/10.1016/j.jhazmat.2023.133303>.
7. Shen, P.; Hou, K.J.; Chen, F.; Pi, Z.J.; He, L.; Chen, S.J.; Li, X.M.; Yang, Q. Ultra-rapid and long-lasting activation of peracetic acid by Cu-Co spinel oxides for eliminating organic contamination: Role of radical and non-radical catalytic oxidation. *Chem. Eng. J.* **2023**, *463*, 13. <https://doi.org/10.1016/j.cej.2023.142344>.
8. Wang, J.W.; Xiong, B.; Miao, L.; Wang, S.L.; Xie, P.C.; Wang, Z.P.; Ma, J. Applying a novel advanced oxidation process of activated peracetic acid by CoFe₂O₄ to efficiently degrade sulfamethoxazole. *Appl. Catal. B-Environ.* **2021**, *280*, 9. <https://doi.org/10.1016/j.apcatb.2020.119422>.
9. Coles, C.A.; Rao, S.R.; Yong, R.N. Lead and cadmium interactions with mackinawite: Retention mechanisms and the role of pH. *Environ. Sci. Technol.* **2000**, *34*, 996-1000. <https://doi.org/10.1021/es990773r>.
10. Csákbérenyi-Malasics, D.; Rodriguez-Blanco, J.D.; Kis, V.K.; Recnik, A.; Benning, L.G.; Pósfai, M. Structural properties and transformations of precipitated FeS. *Chem. Geol.* **2012**, *294*, 249-258. <https://doi.org/10.1016/j.chemgeo.2011.12.009>.
11. Zhang, K.J.; Zhou, X.Y.; Du, P.H.; Zhang, T.Q.; Cai, M.Q.; Sun, P.Z.; Huang, C.H. Oxidation of β-lactam antibiotics by peracetic acid: Reaction kinetics, product and pathway evaluation. *Water Res.* **2017**, *123*, 153-161. <https://doi.org/10.1016/j.watres.2017.06.057>.
12. Grimme, S.; Ehrlich, S.; Goerigk, L. Effect of the damping function in dispersion corrected density functional theory. *J. Comput. Chem.* **2011**, *32*, 1456-1465. <https://doi.org/10.1002/jcc.21759>.
13. Lu, T.; Chen, F.W. Multiwfn: A multifunctional wavefunction analyzer. *J. Comput. Chem.* **2012**, *33*, 580-592. <https://doi.org/10.1002/jcc.22885>.
14. Zhang, J.Y.; Zhao, R.X.; Cao, L.J.; Lei, Y.S.; Liu, J.; Feng, J.; Fu, W.J.; Li, X.Y.; Li, B. High-efficiency biodegradation of chloramphenicol by enriched bacterial consortia: Kinetics study and bacterial community characterization. *J. Hazard. Mater.* **2020**, *384*, 11. <https://doi.org/10.1016/j.jhazmat.2019.121344>.
15. Peng, W.X.; Liao, J.J.; Yan, Y.X.; Chen, L.Q.; Ge, C.J.; Lin, S.W. Enriched nitrogen-doped carbon derived from expired drug with dual active sites as effective peroxymonosulfate activator: Ultra-fast sulfamethoxazole degradation and mechanism insight. *Chem. Eng. J.* **2022**, *446*, 13. <https://doi.org/10.1016/j.cej.2022.137407>.
16. Yi, X.H.; Ji, H.D.; Wang, C.C.; Li, Y.; Li, Y.H.; Zhao, C.; Wang, A.O.; Fu, H.F.; Wang, P.; Zhao, X.; Liu, W. Photocatalysis-activated SR-AOP over PDINH/MIL-88A(Fe) composites for boosted chloroquine phosphate degradation: Performance, mechanism, pathway and DFT calculations. *Appl. Catal. B-Environ.* **2021**, *293*, 14. <https://doi.org/10.1016/j.apcatb.2021.120229>.
17. Liu, H.H.; Zhao, J.; Wang, Y.; Wu, Y.L.; Dong, W.B.; Nie, M.H.; Wang, X.N. Enhancement of peroxymonosulfate activation by sinapic acid accelerating Fe(III)/Fe(II) cycle. *Chem. Eng. J.* **2022**, *446*: 137177. <https://doi.org/10.1016/j.cej.2022.137177>.
18. Li, Y.; Wu, Y.L.; Dong, W.B. Trace catechin enhanced degradation of organic pollutants with activated peroxymonosulfate: Comprehensive identification of working oxidizing species. *Chem. Eng. J.* **2022**, *429*: 132408. <https://doi.org/10.1016/j.cej.2021.132408>.
19. Bi, W.L.; Wu, Y.L.; Dong, W.B. The degradation of oxytetracycline with low concentration of persulfate sodium motivated by copper sulphate under simulated solar light. *Chem. Eng. J.* **2020**, *393*, 122782. <https://doi.org/10.1016/j.cej.2019.122782>.
20. Song, Z.; Zhang, Y.; Zhang, X.; Zhou, X.; Chen, Y.D.; Duan, X.G.; Ren, N.Q. Kinetics study of chloride-activated peracetic acid for purifying bisphenol A: Role of Cl₂/HClO and carbon-centered radicals. *Water Res.* **2023**, *242*, 8. <https://doi.org/10.1016/j.watres.2023.120274>.